



Exciton resonance tuning of an atomically thin lens

Jorik van de Groep^{1,4}, Jung-Hwan Song¹, Umberto Celano^{1,2}, Qitong Li¹, Pieter G. Kik^{1,3} and Mark L. Brongersma¹✉

The highly engineerable scattering properties of resonant optical antennas underpin the operation of metasurface-based flat optics. Thus far, the choice of antenna has been limited to shaped metallic and high-index semiconductor nanostructures that support geometrical plasmonic or Mie resonances. Whereas these resonant elements offer strong light-matter interaction and excellent control over the scattering phase and amplitude, their electrical tunability has proven to be quite limited. Here, we demonstrate how excitonic resonances in atomically thin semiconductors can be harnessed as a different, third type of resonance to create mutable, flat optics. These strong materials-based resonances are unmatched in their tunability with various external stimuli. To illustrate the concept, we first demonstrate how excitons can enhance the focusing efficiency of a millimetre-scale, patterned WS₂ zone plate lens. We also show how electrical gating can completely turn on and off the exciton resonance and thereby modulate the focusing efficiency by 33%.

Ever since the development of diffractive optical elements in the 1970s, researchers have uncovered increasingly sophisticated, fundamental optics principles by which bulky optical elements can be replaced by thin, lightweight counterparts¹. This has recently culminated in a worldwide activity aimed at creating nanophotonic metasurfaces, essentially flat optics composed of dense arrays of metal or semiconductor nanostructures^{2,3}. Such structures facilitate effective control over the local light scattering phase and amplitude by employing plasmonic⁴ or Mie resonances⁵. These two types of resonance have been instrumental in realizing small-form-factor optics delivering multifunctionality^{6,7}, very high numerical apertures^{8,9}, minimal aberrations^{10–12}, nonlinear optics^{13,14} and control over the light field^{15,16}. Despite these impressive advances, metasurface functions have largely remained static. For emerging applications, such as light detection and ranging (LIDAR), dynamic holography, computational imaging and sensing^{17,18}, it would be highly desirable to find ways to electrically activate metasurfaces and achieve dynamic control.

Whereas the importance of plasmonic and Mie resonances in metasurface design cannot be overstated, their use in active metadevices can also prove limiting as they tend to offer only weak electrical tunability. This finds its origin in the limited magnitude of most electroabsorption and electrorefraction effects in metals and semiconductors. It is thus worth considering what other resonances can be utilized in realizing electrically tunable flat optics. From decades of research on optical modulation, it is clear that the strongest, high-speed modulation of materials' optical properties is achieved by manipulating excitons, electron–hole pairs in semiconductors bound by the Coulomb force¹⁹. Their resonant excitation can give rise to sharply peaked absorption features, just below the bandgap of a semiconductor. The associated absorption coefficients can reach levels as high as 1,000 cm⁻¹. In the larger (~100 nm) Mie resonant semiconductor nanostructures used in metasurfaces, the optical material's properties are essentially bulk-like and the exciton binding energy tends to be small (5–10 meV). As a result, the excitonic features are absent at room temperature. In contrast, excitons dominate the near-edge optical properties of two-dimensional (2D) semiconductors, such as the monolayer transition metal dichalcogenides (TMDCs).

The reduced screening in these quantum materials leads to binding energies of hundreds of millielectronvolts and consequently excitons can exist even at room temperature^{20,21}. Exciton resonances can also effectively be tuned over several 100 meV with changes in the material's composition, environmental index^{22–24}, electric/magnetic fields^{22,25} and strain^{26,27}. The suppression of exciton states through carrier injection^{28–30} can have an even stronger impact on the material's optical properties. Based on recent measurements showing near-unity reflectivity from monolayers of MoSe₂ (refs. 31–33), it is also clear that the interaction with a single layer can be extremely strong.

These findings raise the intriguing question whether excitonic resonances can be harnessed to realize electrically tunable and atomically thin metasurface components. Materials with excitonic resonances have already been placed near plasmonic and Mie resonators with the goal of tuning them through strong coupling^{34,35}. A variety of passive optical elements has also been realized by patterning multilayer 2D TMDCs^{36,37}, multilayer graphene³⁸, and 200-nm-thick graphene oxide³⁹, and even small-area, monolayer TMDCs⁴⁰. However, the critical role excitons can play in optical wavefront manipulation has not yet been elucidated and a demonstration of active modulation of atomically thin optical elements has therefore remained elusive.

Here, we demonstrate large-area, actively tunable and atomically thin optical elements by carving them directly out of a monolayer of WS₂. This material displays a strong excitonic resonance in the visible spectral range. Counter to the usual approach of engineering the size and shape of geometrically resonant antennas, the design of metasurfaces made from 2D excitonic materials relies on identifying, engineering, and modifying the material's resonance. Furthermore, in optimizing the spatial arrangement of 2D materials to achieve specific optical functions, it is important to realize that resonant, tunable light–matter interaction is naturally obtained wherever the material is located. These notions open entirely new design strategies for highly tunable flat optics.

Tunable atomically thin zone plate lens

Figure 1a illustrates an atomically thin zone plate lens whose properties can be controlled by electrical gating with an ionic liquid. It is 1 mm in diameter and features a series of 202 concentric rings that

¹Geballe Laboratory for Advanced Materials, Stanford University, Stanford, CA, USA. ²IMEC Leuven, Leuven, Belgium. ³CREOL, The College of Optics and Photonics, University of Central Florida, Orlando, FL, USA. ⁴Present address: Van der Waals–Zeeman Institute for Experimental Physics, Institute of Physics, University of Amsterdam, Amsterdam, Netherlands. ✉e-mail: brongersma@stanford.edu

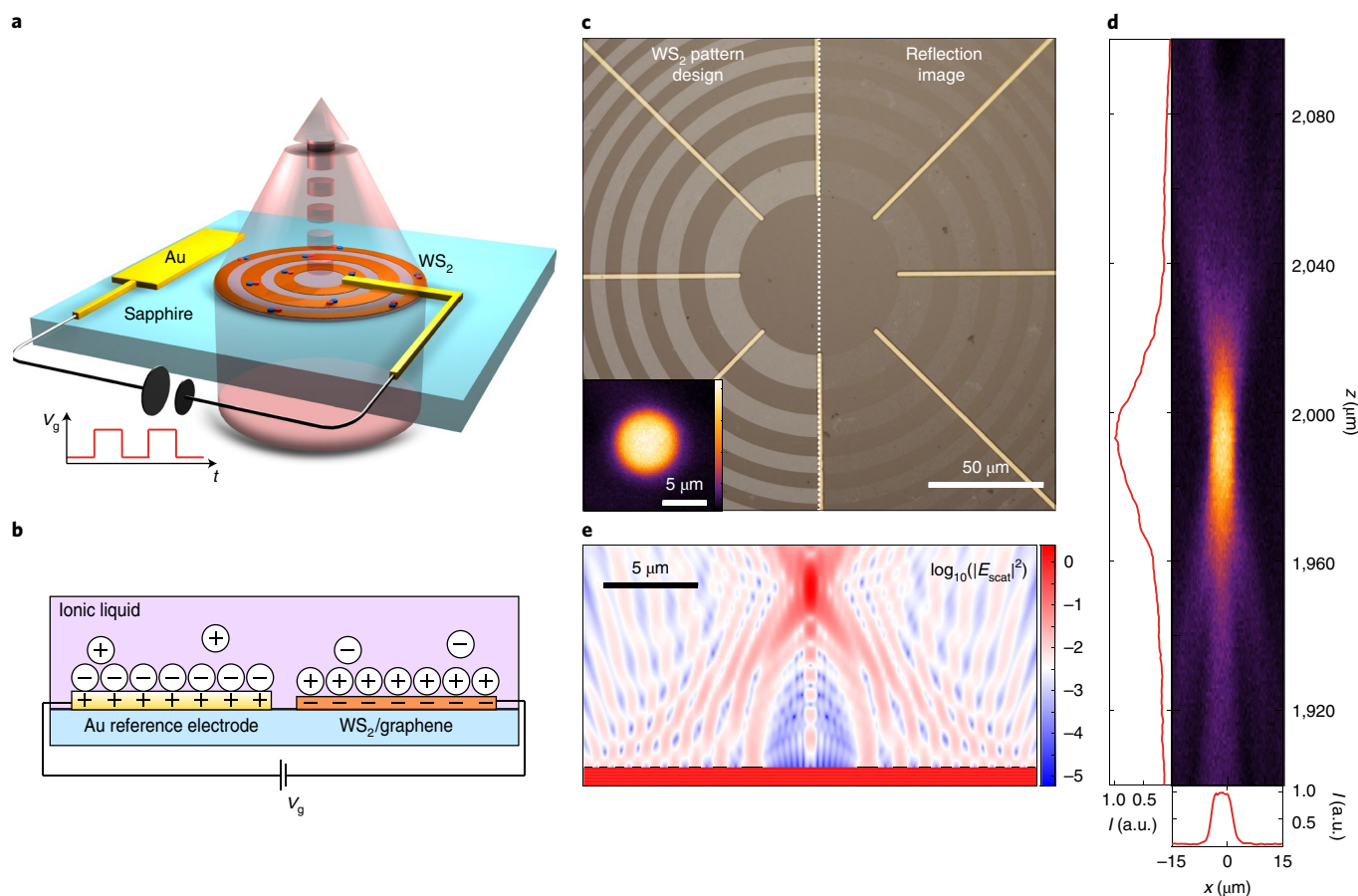


Fig. 1 | Atomically thin and tunable flat lenses. **a**, Schematic of the proposed WS₂ zone plate lens in an electrochemical cell. Time-varying ionic-liquid gate voltages result in a modulation of the focusing efficiency by quenching exciton resonances. **b**, Schematic of the working principle of ionic-liquid gating inside an electrochemical cell. Charged molecules screen the Coulombic potential of the doped WS₂/graphene heterostructure and the Au reference pad. **c**, Optical microscope image of the centre of a fabricated lens (right) and the designed WS₂ pattern overlaid (left, light shaded regions). Inset: x-y scan of the focus formed approximately 2 mm above the patterned surface ($\lambda = 620$ nm). **d**, x-z scan of the focused beam ($\lambda = 620$ nm). Cross-sections of the normalized intensity along the z axis of the focused beam and x axis (for $z = 1,993$ μm) are also shown in arbitrary units (a.u.). **e**, Scattered field intensity ($\lambda = 620$ nm) behind a 20- μm -diameter zone plate lens with a focal length $f = 10$ μm on sapphire (\log_{10} colour scale).

are patterned into a monolayer of WS₂ grown by chemical vapour deposition (CVD) on sapphire. The design of the ring diameter and spacing is conceptually similar to that of a conventional zone plate and aims to achieve constructive interference of the diffracted light from the WS₂ rings into a sharp focus. Figure 1c presents the centre part of the zone plate lens (see Supplementary Figs. 1, 4 and 5 for atomic force microscope (AFM) topography, large-area microscope image and Raman analysis, respectively). To facilitate dynamic electrical control over the lens properties, we found that it is beneficial to transfer a large-area graphene monolayer on top of the WS₂ as a transparent electrode. The graphene facilitates enhanced d.c. surface conductivity and warrants uniform gating of the WS₂ (Supplementary Fig. 1). It also serves as a protective layer for the WS₂ in the electrochemical gating experiments and enhances long-term stability. It is known that monolayer graphene does not fully screen gate-induced electric fields, allowing effective doping of the underlying WS₂ (ref. 41). A total of eight gold radial finger-electrodes are applied to bias the lenses. Finally, we place an optically transparent electrochemical cell filled with ionic liquid (diethylmethyl(2-methoxyethyl)ammonium bis(trifluoromethylsulfonyl)imide (DEME-TFSI)) on top (Fig. 1b and Supplementary Fig. 2). See Methods and Supplementary Fig. 3 for details on the sample fabrication.

When the lens is bottom-illuminated with 620 nm light, we can use confocal scanning microscopy (Supplementary Fig. 6) to

characterize the shape and intensity of the focused beam. A clear focal spot is observed (Fig. 1c inset) behind the lens with a characteristic flat-top beam profile that is well described by a super-Gaussian line shape⁴² (Supplementary Fig. 7) with a full-width at half-maximum of 6.7 μm . The spot size and shape result from the experimental illumination conditions. The measured focal length is slightly shorter than the free-space design of 2 mm due to the presence of the electrochemical cell (Fig. 1d).

To highlight the important role exciton resonances can play in the operation of the flat lens, it is of value to view the rings of WS₂ as sources of scattered fields, driven by an incident plane wave. The locally generated scattered fields are proportional to the polarization $\mathbf{P} = \epsilon_0 \chi \mathbf{E}_i$ of the WS₂ material, where ϵ_0 is the permittivity of free space, χ is the complex electric susceptibility and \mathbf{E}_i is the local driving electric field. The spectral behaviour of χ is thus encoded into the spectral dependence of the amplitude and phase of the scattered fields. The strongest scattering is therefore expected near the exciton resonance where the magnitude of χ is largest and we explore this situation first. Figure 1e shows a scattered field simulation that illustrates the focusing action of a 20- μm -diameter WS₂ zone plate lens illuminated at the exciton resonance wavelength ($\lambda = 620$ nm). Using room-temperature literature values for exfoliated WS₂ (ref. 43) for χ we find a focusing efficiency of 0.08%. Substantially higher focusing efficiencies could be reached with higher-quality exfoliated

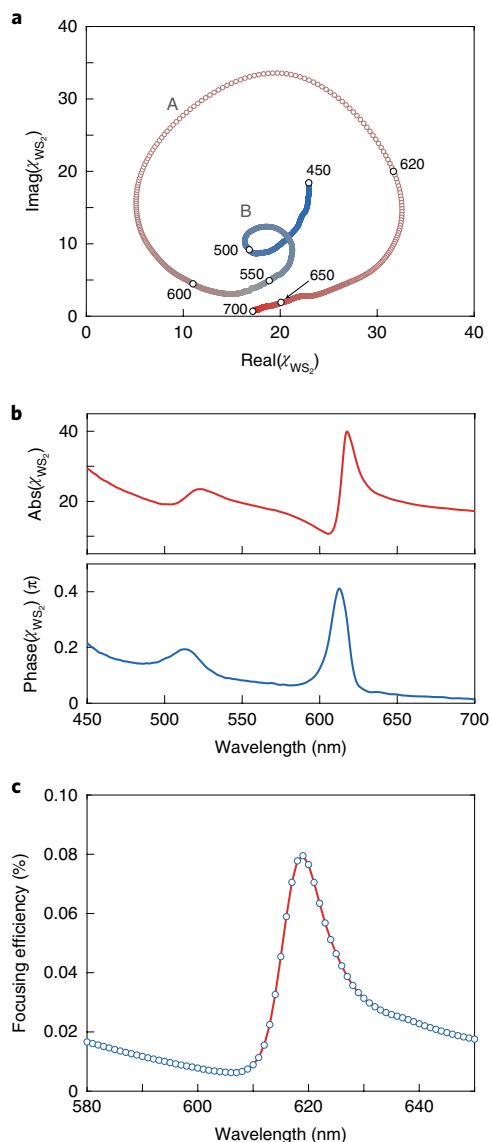


Fig. 2 | Material susceptibility and focusing efficiency. **a**, Phasor plot of the complex susceptibility of WS_2 . The white dots and numbers indicate the corresponding wavelengths. A and B refer to the exciton resonances. **b**, Absolute value (top) and phase angle (bottom) of the material susceptibility. **c**, Simulated focusing efficiency spectrum of the scattered light for the 20- μm -diameter zone plate lens shown in Fig. 1e.

materials and at low temperatures for which the exciton linewidth is noticeably reduced^{31–33}. Even at these low diffraction efficiencies these lenses can have important applications in free-space optical beam tapping and sensing⁴⁴. Whereas the current lens is virtually invisible to the human eye for non-resonant wavelengths, it can capture important information from its surroundings and the intensity in the focus well exceeds the intensity of the incident plane wave (by a factor 2.75) as the light is concentrated by the ratio of the lens area to the focal spot size of about 10^3 . This factor is for the simulated 20- μm -diameter lens and substantially larger concentration is achieved with our millimetre-sized, fabricated lenses.

The spectral dependence of the focusing efficiency is intrinsically linked to the complex material susceptibility χ of the WS_2 monolayer. Using literature values for χ (ref. 43), we find that the susceptibility near the A and B exciton resonances appears as loops in the complex plane with radii proportional to the oscillator strength

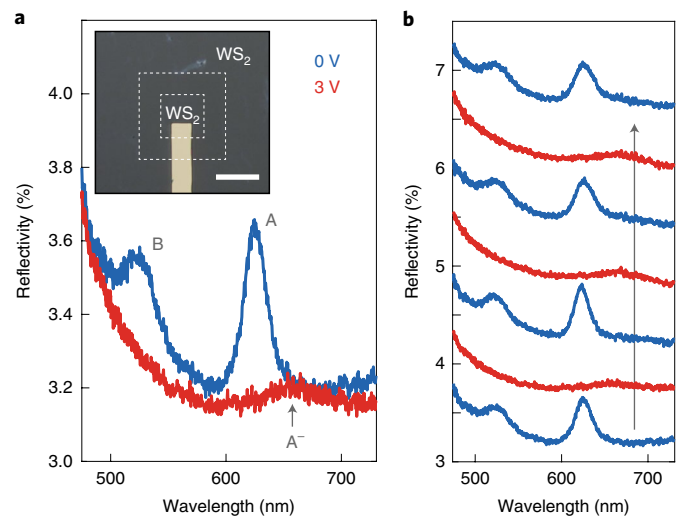


Fig. 3 | Exciton manipulation through ionic-liquid gating. **a**, Reflectivity spectra of a $20 \times 20 \mu\text{m}^2$ isolated patch of WS_2 for $V_g = 0\text{ V}$ (blue) and gated at $V_g = 3\text{ V}$ (n-doping, red). Inset: optical microscope image of the patch device. The WS_2 in between the dashed lines is removed, isolating the inner WS_2 area. Scale bar, 20 μm . **b**, Reflectivity spectra while cycling between the neutral (blue) and doped state (red) showing high reproducibility. Sequentially obtained spectra are offset for clarity, as indicated by the grey arrow.

of each resonance (Fig. 2a). As a result, the resonances not only give rise to a strong oscillation in the magnitude of χ , but also a notable change in the phase angle up to $\sim 0.4\pi$ around $\lambda = 617\text{ nm}$ (Fig. 2b). In the absence of the direct substrate transmission, the scattered light intensity in the focus of the 20- μm -diameter WS_2 zone plate lens (as obtained from Fig. 1e) also shows an asymmetric line shape that is governed by the WS_2 material susceptibility squared (Fig. 2c). Experimentally, the scattered fields cannot be isolated, and the spectral line shape results in general from interference with the direct substrate transmission. However, by collecting the weakly scattered light from a large area (1 mm diameter), the focal intensity of our experimental zone plates is high and largely determined by the scattered fields from the WS_2 material.

Exciton resonance tuning

The possibility to modulate the focusing efficiency of our lens stems from our ability to alter the exciton resonances of the WS_2 material via electrical gating. We first analyse the induced reflectivity changes from a simple square $20 \times 20 \mu\text{m}^2$ isolated patch of monolayer WS_2 (Fig. 3a inset) as a function of applied gate voltage. As expected, the reflection spectrum is dominated by the B and A excitons at $\lambda = 520\text{ nm}$ and $\lambda = 625\text{ nm}$, respectively. Note that the linewidth of the main reflection peak ($\sim 75\text{ meV}$) is notably larger than reported for exfoliated flakes⁴³, quite common for lower-quality, large-area CVD-grown WS_2 monolayers. The main excitonic reflection peak is completely suppressed and a small, redshifted peak at $\lambda = 655\text{ nm}$ is observed when a 3 V gate bias is applied to induce n-type doping. The suppression and redshift of the A exciton result from a screening of the electron–hole interaction due to the increased electron density and an interconversion to negatively charged exciton states (A^- trions)^{30,45}. A similarly strong suppression is observed for the B exciton located at $\lambda = 520\text{ nm}$. The observed complete removal of the excitonic resonances is known to produce one of the largest possible changes in the susceptibility¹⁹. The exciton suppression is also fully reversible and highly reproducible (Fig. 3b). These observations highlight the benefits of excitonic resonances over plasmonic and Mie-type resonances, which are much harder to tune or quench.

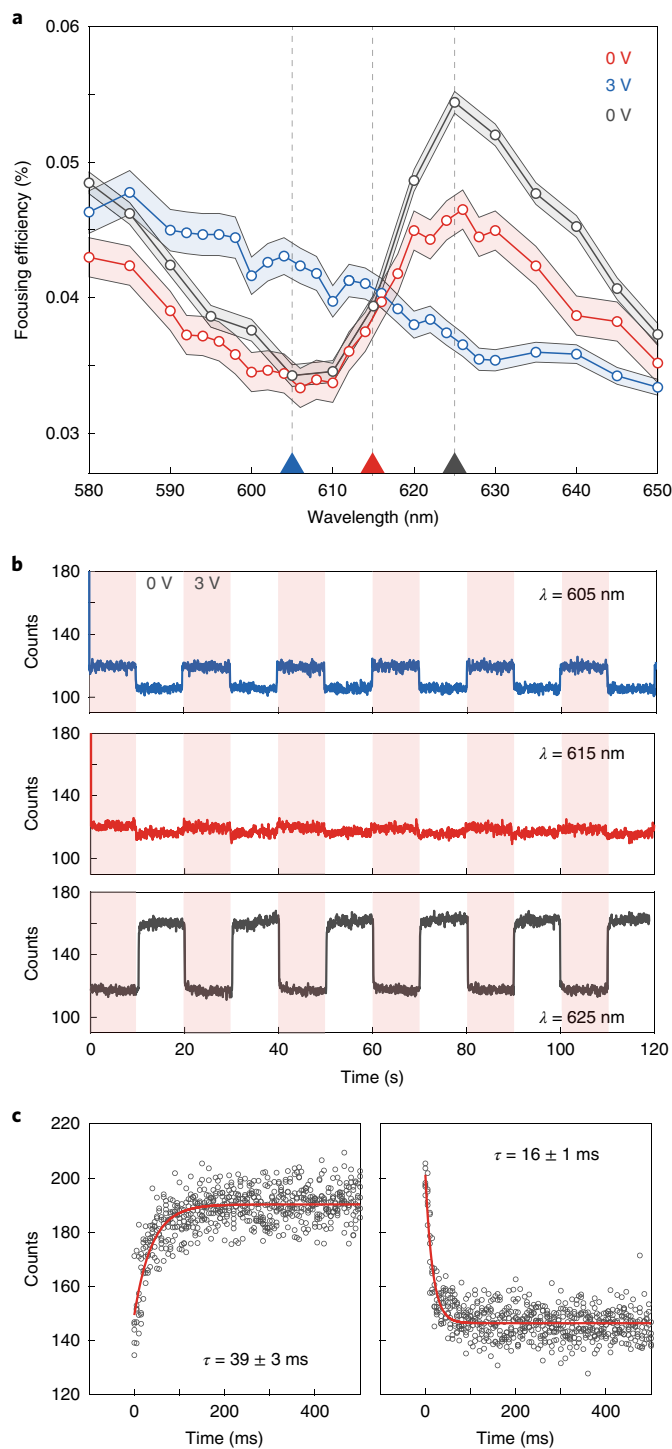


Fig. 4 | Exciton modulation of the intensity in the focus. **a**, Focusing efficiency spectra of the zone plate lens in pristine (red, $V_g = 0$ V), gated (blue, $V_g = 3$ V) and restored state (grey, $V_g = 0$ V). The shaded area indicates the error bar corresponding to one standard deviation. The triangles at the bottom axis and dashed lines indicate the wavelengths used for **b**. **b**, Intensity in the focus as a function of time for $\lambda = 605$ nm (blue, top), for $\lambda = 615$ nm (red, middle) and for $\lambda = 625$ nm (grey, bottom) while V_g is cycled between 0 V (white background) and 3 V (red background). **c**, Time trace of rise (left) and fall (right) of the focal intensity for $\lambda = 625$ nm. The corresponding rise and fall times obtained from a fit (red) are also shown.

Focal intensity modulation

Next, we will capitalize on the large tunability of the exciton resonances to modulate the intensity in the focal spot of a lens. We experimentally measure the power in the focus as a function of wavelength and normalize to the power incident on the zone plate lens to determine the focusing efficiency spectrum (see Methods for procedure). A clear asymmetric line shape is observed for the pristine zone plate lens (Fig. 4a, red), closely matching the calculated response in Fig. 2c that omitted the directly transmitted light. This correspondence is a clear indication that the focused excitonic light scattering dominates the direct substrate transmission. Next, we apply a 3 V gate bias (V_g) to the WS₂/graphene heterostructure to suppress the exciton resonance. The asymmetric excitonic line is fully suppressed (Fig. 4a, blue) and a flat non-resonant efficiency spectrum is clearly observed. Note that slight over-etching into the substrate during the sample fabrication (~ 15 nm; Supplementary Fig. 1) gives rise to non-resonant background focusing (Supplementary Fig. 8). Finally, we use the reversible switching of the exciton resonance to restore the neutral resonant state (Fig. 4a, grey). The distinctive asymmetric resonant line shape is reproduced, with an enhanced amplitude that corresponds to an increase in oscillator strength and reduction in exciton linewidth. This is consistent with observations of linewidth narrowing in reflection measurements on our patch devices (such as Fig. 3a) upon the first gating cycle (Supplementary Fig. 9). We attribute this effect to the passivation of positively charged intrinsic and fabrication-induced defects during the first gating cycle. We note that the measured focusing efficiency is relatively low ($<0.1\%$) and is primarily limited by the relatively low material quality of the commercial WS₂. Recent experiments on small flakes of MoSe₂ have demonstrated that high-quality encapsulated monolayers can achieve an optical reflectance of $\sim 80\%$ ^{31–33}. Improvements in the large-area growth of high-quality monolayer TMDCs will therefore strongly enhance the focusing efficiencies (see Supplementary Note 1 and Supplementary Figs. 10 and 11 for an analysis of the potential efficiencies and future improvements of flat optics based on 2D semiconductors).

Using room-temperature, large-area active manipulation of the exciton resonance, we demonstrate dynamic light intensity modulation in the focus of the 2D material zone plate lens (Fig. 4b). Reproducible switching between the exciton-dominated ($V_g = 0$ V) and the exciton-quenched ($V_g = 3$ V) states enables active control over excitonic light scattering amplitude (Fig. 4b). The asymmetric exciton resonance line shape in the focusing efficiency gives rise to decreased ($\lambda = 605$ nm) or increased ($\lambda = 625$ nm) intensity in the focus compared with the non-resonant state. For $\lambda = 615$ nm the efficiency curves intersect (Fig. 4a) however, which results in no observable contrast (Fig. 4b). The maximum modulation depth observed is $\sim 33\%$ for $\lambda = 625$ nm, despite the single-pass interaction of light with the atomically thin structure. In our current sample, the modulation depth is limited by non-resonant background focusing as a result of the gently over-etched pattern (Supplementary Fig. 8). The typical device response time is characterized from accumulated time traces (5 ms resolution) of the focal intensity for $\lambda = 625$ nm. The rise and fall time are measured to be 39 ± 3 ms and 16 ± 1 ms, respectively. The response time and asymmetry are a result of the ion-transport-limited complex formation and disassembly of the ionic-liquid electrical double layer⁴⁶. Implementing solid-state gating schemes rather than ionic-liquid gating would increase the device response time by orders of magnitude and is merely limited by fabrication challenges.

Conclusions

The presented results demonstrate the important role of excitonic material resonances in the operation of atomically thin optical lenses. More advanced gating schemes with local and interleaved gating electrodes will enable excitonic optical devices with more

complex tunable functionalities including tunable focal lengths or beam steering. The highly tunable nature of these excitonic material resonances opens an entirely new approach for the design of dynamic flat optics and metasurfaces with applications in free-space beam tapping, wavefront manipulation, spectral polarimetry and augmented/virtual reality (Supplementary Note 2).

Online content

Any methods, additional references, Nature Research reporting summaries, source data, extended data, supplementary information, acknowledgements, peer review information; details of author contributions and competing interests; and statements of data and code availability are available at <https://doi.org/10.1038/s41566-020-0624-y>.

Received: 3 October 2019; Accepted: 19 March 2020;

Published online: 27 April 2020

References

- Lalanne, P. & Chavel, P. Metalenses at visible wavelengths: past, present, perspectives. *Laser Photon. Rev.* **11**, 1600295 (2017).
- Chen, H. T., Taylor, A. J. & Yu, N. A review of metasurfaces: physics and applications. *Rep. Prog. Phys.* **79**, 076401 (2016).
- Khorasaninejad, M. & Capasso, F. Metalenses: versatile multifunctional photonic components. *Science* **358**, eaam8100 (2017).
- Yu, N. et al. Light propagation with phase discontinuities: generalized laws of reflection and refraction. *Science* **334**, 333–337 (2011).
- Lin, D., Fan, P., Hasman, E. & Brongersma, M. L. Dielectric gradient metasurface optical elements. *Science* **345**, 298–302 (2014).
- Kamali, S. M. et al. Angle-multiplexed metasurfaces: encoding independent wavefronts in a single metasurface under different illumination angles. *Phys. Rev. X* **7**, 041056 (2017).
- Maguid, E. et al. Multifunctional interleaved geometric-phase dielectric metasurfaces. *Light Sci. Appl.* **6**, e17027 (2017).
- Paniagua-Domínguez, R. et al. A metalens with a near-unity numerical aperture. *Nano Lett.* **18**, 2124–2132 (2018).
- Liang, H. et al. Ultrahigh numerical aperture metalens at visible wavelengths. *Nano Lett.* **18**, 4460–4466 (2018).
- Khorasaninejad, M. et al. Metalenses at visible wavelengths: diffraction-limited focusing and subwavelength resolution imaging. *Science* **352**, 1190–1194 (2016).
- Shrestha, S., Overvig, A. C., Lu, M., Stein, A. & Yu, N. Broadband achromatic dielectric metalenses. *Light Sci. Appl.* **7**, 85 (2018).
- Wang, S. et al. A broadband achromatic metalens in the visible. *Nat. Nanotechnol.* **13**, 227–232 (2018).
- Li, G., Zhang, S. & Zentgraf, T. Nonlinear photonic metasurfaces. *Nat. Rev. Mater.* **2**, 17010 (2017).
- Krasnok, A., Tymchenko, M. & Alù, A. Nonlinear metasurfaces: a paradigm shift in nonlinear optics. *Mater. Today* **21**, 8–21 (2018).
- Lin, R. J. et al. Achromatic metalens array for full-colour light-field imaging. *Nat. Nanotechnol.* **14**, 227–231 (2019).
- Holsteen, A. L., Lin, D., Kauvar, I., Wetzstein, G. & Brongersma, M. L. A light-field metasurface for high-resolution single-particle tracking. *Nano Lett.* **19**, 2267–2271 (2019).
- Schwarz, B. LIDAR: mapping the world in 3D. *Nat. Photon.* **4**, 429–430 (2010).
- Jung, I. W. et al. 2-D MEMS scanner for handheld multispectral confocal microscopes. In *2012 Int. Conf. on Optical MEMS and Nanophotonics* 238–239 (IEEE, 2012).
- Miller, D. A. B. Attojoule optoelectronics for low-energy information processing and communications. *J. Light. Technol.* **35**, 346–396 (2017).
- Mak, K. F., Lee, C., Hone, J., Shan, J. & Heinz, T. F. Atomically thin MoS₂: a new direct-gap semiconductor. *Phys. Rev. Lett.* **105**, 136805 (2010).
- Cao, L. Two-dimensional transition-metal dichalcogenide materials: toward an age of atomic-scale photonics. *Mater. Res. Soc. Bull.* **40**, 592–599 (2015).
- Stier, A. V., Wilson, N. P., Clark, G., Xu, X. & Crooker, S. A. Probing the influence of dielectric environment on excitons in monolayer WSe₂: insight from high magnetic fields. *Nano Lett.* **16**, 7054–7060 (2016).
- Raja, A. et al. Coulomb engineering of the bandgap and excitons in two-dimensional materials. *Nat. Commun.* **8**, 15251 (2017).
- Gupta, G., Kallatt, S. & Majumdar, K. Direct observation of giant binding energy modulation of exciton complexes in monolayer MoSe₂. *Phys. Rev. B* **96**, 081403 (2017).
- Stier, A. V. et al. Magneto-optics of exciton Rydberg states in a monolayer semiconductor. *Phys. Rev. Lett.* **120**, 057405 (2018).
- Lloyd, D. et al. Band gap engineering with ultralarge biaxial strains in suspended monolayer MoS₂. *Nano Lett.* **16**, 5836–5841 (2016).
- Aslan, O. B., Deng, M. & Heinz, T. F. Strain tuning of excitons in monolayer WSe₂. *Phys. Rev. B* **98**, 115308 (2018).
- Ross, J. S. et al. Electrical control of neutral and charged excitons in a monolayer semiconductor. *Nat. Commun.* **4**, 1474 (2013).
- Chernikov, A. et al. Electrical tuning of exciton binding energies in monolayer WS₂. *Phys. Rev. Lett.* **115**, 126802 (2015).
- Yu, Y. et al. Giant gating tunability of optical refractive index in transition metal dichalcogenide monolayers. *Nano Lett.* **17**, 3613–3618 (2017).
- Mak, K. F. & Shan, J. Mirrors made of a single atomic layer. *Nature* **556**, 177–178 (2018).
- Back, P., Zeytinoglu, S., Ijaz, A., Kroner, M. & Imamoglu, A. Realization of an electrically tunable narrow-bandwidth atomically thin mirror using monolayer MoSe₂. *Phys. Rev. Lett.* **120**, 037401 (2018).
- Scuri, G. et al. Large excitonic reflectivity of monolayer MoSe₂ encapsulated in hexagonal boron nitride. *Phys. Rev. Lett.* **120**, 037402 (2018).
- Krasnok, A., Lepeshov, S. & Alù, A. Nanophotonics with 2D transition metal dichalcogenides. *Opt. Express* **26**, 15972–15994 (2018).
- Tserkezis, C. et al. Mie excitons: understanding strong coupling in dielectric nanoparticles. *Phys. Rev. B* **98**, 155439 (2018).
- Yang, J. et al. Atomically thin optical lenses and gratings. *Light Sci. Appl.* **5**, e16046 (2016).
- Liu, C. H. et al. Ultrathin van der Waals metalenses. *Nano Lett.* **18**, 6961–6966 (2018).
- Kong, X. T. et al. Graphene-based ultrathin flat lenses. *ACS Photon.* **2**, 200–207 (2015).
- Zheng, X. et al. Highly efficient and ultra-broadband graphene oxide ultrathin lenses with three-dimensional subwavelength focusing. *Nat. Commun.* **6**, 8433 (2015).
- Lin, H., Xu, Z. Q., Qiu, C., Jia, B. & Bao, Q. High performance atomically thin flat lenses. Preprint at <https://arxiv.org/abs/1611.06457> (2016).
- Georgiou, T. et al. Vertical field-effect transistor based on graphene-WS₂ heterostructures for flexible and transparent electronics. *Nat. Nanotechnol.* **8**, 100–103 (2012).
- Shealy, D. L. & Hoffnagle, J. A. Laser beam shaping profiles and propagation. *Appl. Opt.* **45**, 5118–5131 (2006).
- Li, Y. et al. Measurement of the optical dielectric function of monolayer transition-metal dichalcogenides: MoS₂, MoSe₂, WS₂, and WSe₂. *Phys. Rev. B* **90**, 205422 (2014).
- Li, Q. T. et al. Free-space optical beam tapping with an all-silica metasurface. *ACS Photon.* **4**, 2544–2549 (2017).
- Lien, D. H. et al. Electrical suppression of all nonradiative recombination pathways in monolayer semiconductors. *Science* **364**, 468–471 (2019).
- Leighton, C. Electrolyte-based ionic control of functional oxides. *Nat. Mater.* **18**, 13–18 (2019).

Publisher's note Springer Nature remains neutral with regard to jurisdictional claims in published maps and institutional affiliations.

© The Author(s), under exclusive licence to Springer Nature Limited 2020

Methods

Sample fabrication. The bracketed numbers in the text below refer to the step number in Supplementary Fig. 3, which schematically shows the fabrication steps. (1) $1 \times 1 \text{ cm}^2$ CVD-grown monolayer WS_2 on sapphire was obtained commercially (2D semiconductors), cleaned with solvents and baked at 100°C for 3 min. (2) Large-area commercially obtained monolayer graphene (ACSMaterial Trivial Transfer Graphene) was placed on top of the WS_2 to form a WS_2 /graphene bilayer using wet-transfer techniques. The sample was dried by annealing in a tube oven at 100°C in a nitrogen atmosphere for 1 h. (3) Gold micrometre-scale contact lines, pads and markers were fabricated by maskless photolithography using a Heidelberg MLA 150 direct-write lithography tool. The sample was coated with vapour-phase hexamethyldisilazane (HMDS) using an oven (Yield Engineering Systems) to promote photoresist adhesion. Next, photoresist (PR3612) was spin-coated, baked, exposed at 80 mJ cm^{-2} , post-baked and developed using MIF-26A developer. (4) A 15 s O_2 descum plasma etch was used to remove any residual photoresist from the trenches, followed by deposition of 5 nm Ti and 100 nm Au through electron-beam evaporation. Lift-off was performed by soaking in acetone and 5 s of ultrasonication, followed by solvent cleaning. (5) Using low-resolution electron-beam lithography, we patterned the lens outline into the bilayer, thereby isolating the zone plates electrically. To do this, the sample was immersed in HMDS primer (SURPASS 3000), baked, and coated with negative-tone resist (maN-2405) diluted at 1:2 volume ratio with methoxybenzene (anisole), exposed, and developed in MF-319 developer. (6) CF_4 -based reactive-ion etching was used to etch the non-covered graphene and WS_2 , followed by resist stripping in acetone and solvent cleaning. (7) Next, the zone plate pattern was fabricated using electron-beam lithography. Poly(methyl methacrylate) (PMMA, 495PMMA A4) was spin-coated, baked, exposed and developed in a mixture of methyl isobutyl ketone (MIBK) and isopropanol (IPA), MIBK:IPA 1:1. (8) The zone plate pattern was then transferred into the WS_2 /graphene bilayer using CF_4 -based reactive-ion etching, and the PMMA was stripped using overnight immersion in acetone. (9) We then fabricated an optically transparent electrochemical cell on top. We placed $\sim 150\text{-}\mu\text{m}$ -wide strips of thermoplastic ($\sim 60\text{-}\mu\text{m}$ thick, Solaronix Meltonix 1170–60) along the sides of the sample, and placed a cover glass on top (type no. 1). Heating the thermoplastic to 130°C on a hot plate sealed the cover glass in place, creating an open channel. (10) Finally, we filled the cell with DEME-TFSI ionic liquid, and sealed the two openings using epoxy.

For the optical measurements, the sample was mounted and wire-bonded onto a custom-made printed circuit board that had an opening to enable optical transmission measurements (Supplementary Fig. 2).

Reflection measurements. In situ reflection measurements (Fig. 3) were performed using a Nikon C2 confocal microscope. Unpolarized light from a halogen lamp illuminated the sample through a $\times 50$ long working distance objective (Nikon LU Plan ELWD numerical aperture (NA) = 0.55). Broadband wide-field illumination was used, with the aperture stop closed to obtain minimally focused excitation with angles of incidence close to normal. The reflection signal was collected by a confocal scanner with a $60\text{-}\mu\text{m}$ pinhole and analysed using a SpectraPro 2300i spectrometer ($150 \text{ lines mm}^{-1}$, blazed for $\lambda = 500 \text{ nm}$) and a Pixis Si charge-coupled device (CCD; -70°C detector temperature). The reported spectra are the average of 100 frames (0.5 s integration time each). The spectra are normalized to the reflection spectrum of a protected silver mirror (Thorlabs, PF10-03-P01).

AFM and conductive AFM measurements. AFM measurements (Supplementary Fig. 1) were performed using a Park XE-100 in tapping mode equipped with NSC15/AL BS from Mikromasch (spring constant 40 N m^{-1}). For the conductive AFM measurements conductive Cr–Au coated probes were used in contact mode (NSC18/Cr–Au, Mikromasch). The current was sensed with a variable-gain, low-noise FEMTO current amplifier (DLPCA-200) that covers a large current amplification range (transimpedance gain from 10^3 to 10^{11} V A^{-1}). The FEMTO amplifier was connected in series with the tip while the bias (2–4 V) was applied to the sample.

Raman characterization. All Raman measurements (Supplementary Fig. 5) were performed using a Horiba Scientific LabRAM HR Evolution spectrometer. A 532-nm pump laser was focused to a diffraction-limited spot using a $\times 100$ objective. A $30\text{-}\mu\text{m}$ confocal pinhole was used and the Raman signal was spectrally dispersed using a grating with $1,800 \text{ lines mm}^{-1}$. Each spectrum is an average of 12 spectra with 5 s integration time, and the dark background signal is subtracted. For the line scan, a 250-ms integration time and a 250-nm step size were used.

Focusing efficiency measurements. The focusing efficiency measurements (Fig. 4a) were performed using a WiTec $\alpha 300$ confocal microscope (Supplementary Fig. 6). A supercontinuum laser and acousto-optic tunable filter (both Fianium) were used to generate monochromatic light ($\sim 5 \text{ nm}$ bandwidth). The laser light was coupled into a $105\text{-}\mu\text{m}$ -diameter multimode fibre to feed the light into the experimental set-up. After outcoupling, the light was collimated (focal length $f = 11 \text{ mm}$) and used to illuminate the sample from below through the substrate.

The focus formed above the surface was mapped confocally using a piezo stage to scan the sample through the focus of a $\times 50$ objective (Zeiss Epiplan HD NA = 0.7). The collected light was coupled into a $25\text{-}\mu\text{m}$ -diameter core collection fibre that functions as the confocal pinhole and analysed using a fibre-coupled avalanche photodiode (APD; Micro Photon Devices). The typical scan range was $15 \times 15 \text{ }\mu\text{m}^2$ with a 200-nm step size, and 25-ms integration time. The electrical bias was applied using a Keithley 2612 sourcemeter.

We determined the focusing efficiency in five steps. First, a 2D super-Gaussian was fitted to the focal shape (see Supplementary Fig. 7 for example cross-cut), which also gives the background intensity. The analytical super-Gaussian function was then spatially integrated without the background contribution to obtain the power in the focus. Second, we removed the sample and mapped the (uniform) intensity in the laser spot for a central wavelength ($\lambda = 610 \text{ nm}$), and spatially averaged the count rate. Third, we measured the laser power incident on the sample $P_{\text{laser}}(\lambda)$ using a calibrated power meter for all wavelengths (including $\lambda = 610 \text{ nm}$). Fourth, we took the ratio of the averaged power measured using the APD and the calibrated power meter at $\lambda = 610 \text{ nm}$. This gave the wavelength-independent system collection efficiency η_{coll} (units counts W^{-1}). Finally, we obtained the power incident on the zone plate as measured by the APD as $\eta_{\text{coll}} P_{\text{laser}}(\lambda) A_{\text{zp}}$, where A_{zp} is the surface area of the zone plate. The efficiency was obtained by the ratio of the integrated intensity in the focus and integrated intensity incident on the zone plate.

The error bars (shaded area in Fig. 4a) represent the uncertainty that is caused by the spatial inhomogeneity of the light directly transmitted by the substrate. Other potential sources of error—such as the uncertainty in the focal position (z coordinate used for the focal mapping) and the fitting error—were evaluated and give negligible error bars. The uncertainty in the input intensity was obtained by comparing the measured laser power spectrum and the background intensity from the 2D super-Gaussian fit to the focus. These both represent the input intensity and should therefore follow the same trend. The error was calculated by taking the standard deviation between the two curves and applying this as the error in the input intensity.

Time-modulation measurements. The time-dependent intensity measurements (Fig. 4b,c) were recorded using the same equipment as the focusing efficiency measurements. Here, the focus position was determined once by confocal mapping. Next, the collection spot was positioned at the centre of the focus, and the APD count rate was recorded as a function of time. For Fig. 4b, a 50-ms integration time was used and the signal was normalized by the laser power to enable direct comparison of the APD count rates. The d.c. bias was cycled between $V_g = 0 \text{ V}$ and $V_g = 3 \text{ V}$ manually every 10 s. For Fig. 4c, a 5-ms integration time was used.

Full-field simulations. Full-field simulations of the scattered field (Figs. 1e and 2c) were performed using commercial finite-difference time-domain simulations (Lumerical). A $20\text{-}\mu\text{m}$ -diameter zone plate was simulated as an infinitely thin 2D object with an optical surface conductivity given by

$$\sigma_s = -i(\epsilon(E) - 1)\omega\epsilon_0 d,$$

with $\epsilon(E)$ the dispersive optical constants taken from ref. ⁴³, ω the angular frequency, and $d = 6.5 \text{ \AA}$ the monolayer thickness. A total-field scattered-field source ($\lambda = 570\text{--}670 \text{ nm}$) illuminates the zone plate with a plane wave, launched from within the semi-infinite sapphire substrate (simulated as a homogeneous non-dispersive medium with refractive index $n = 1.77$). The scattered field above the substrate (Fig. 1e) was recorded by a field monitor. The simulated mesh is uniform, and the mesh resolution is 20 nm. To determine the focusing efficiency (Fig. 2c), a Gaussian line shape was fitted to the focal shape and integrated to determine the total power in the focus. Next, the integrated signal was normalized by the power incident on the zone plate from within the substrate.

Data availability

The data that support the plots within this paper and other findings of this study are available from the corresponding author upon reasonable request.

Acknowledgements

We gratefully acknowledge useful discussions with M. Gebbie. This work was supported by the US Air Force (grant no. AnchorFA9550-17-1-0331). Some of the optical measurements were funded by the DOE 'Photonics at Thermodynamic Limits' Energy Frontier Research Center under grant DE-SC0019140. J.v.d.G. was also supported by a Rubicon Fellowship from the 'Nederlandse Organisatie voor Wetenschappelijk Onderzoek (NWO)'. J.-H.S. was supported by Basic Science Research Program through the National Research Foundation of Korea (NRF) funded by the Ministry of Education (NRF-2016R1A6A3A03012480). U.C. acknowledges the partial support from the Fonds voor Wetenschappelijk Onderzoek—Vlaanderen (FWO). Part of this work was performed at the Nano@Stanford labs, supported by the National Science Foundation under award ECCS-1542152.

Author contributions

J.v.d.G. and M.L.B. conceived the concepts behind this research. J.v.d.G. and J.-H.S. fabricated the samples and performed the optical measurements.

U.C. performed the (conductive) AFM measurements. J.v.d.G., J.-H.S., Q.L., P.G.K. and M.L.B. performed the data analysis and calculations. All authors contributed to writing the manuscript.

Competing interests

The authors declare no competing interests.

Additional information

Supplementary information is available for this paper at <https://doi.org/10.1038/s41566-020-0624-y>.

Correspondence and requests for materials should be addressed to M.L.B.

Reprints and permissions information is available at www.nature.com/reprints.